Research Article

Tao Cheng, Yukuan Ma, Huanhuan Zhao, Tianhao Fei, Linhua Liu* and Jia-Yue Yang*

Dynamic tuning of optical absorbance and structural color of VO_2-based metasurface

https://doi.org/10.1515/nanoph-2023-0169
Received March 10, 2023; accepted May 22, 2023;
published online June 12, 2023

Abstract: Vanadium dioxide (VO_2) is an attractive thermal-control material exhibiting low thermal hysteresis and excellent temperature cycling performance. However, the deficiencies including weak spectral shift and narrow-band absorption during insulating-metallic transitions hinder its application in optoelectronics. The transition metal dichalcogenides (TMDs) can provide a promising solution with their high dielectric properties and robust optical coupling. Here, we report a MoS_2/VO_2/Au/Si metasurface and investigate the dynamic tunability of its optical absorbance and structural color upon heating via spectroscopic ellipsometry measurements and numerical simulations. The first-principles calculations reveal that the dielectric absorptions of metallic and insulating VO_2 oppositely response to temperature, closely related to the difference in the transitions of O-2p states. Finite-element simulations reveal that the introduction of MoS_2 nanostructure induces more absorption peaks by 2∼3 and achieves strong absorption in the full wavelength range of visible light. The Fabry–Perot (F–P) resonance is the critical factor for the optimized optical absorption. The structural color is sensitive to environmental perturbations at high-ε state of VO_2, lower oblique incidence angles, and heights of MoS_2. This work seeks to facilitate the spectral modulation of phase change metamaterials and can be extended to photoelectric detection and temperature sensing applications.

Keywords: dynamic tuning; Fabry–Perot resonance; metasurface; phase change materials; structural color; transition metal dichalcogenides

1 Introduction

Optical metasurfaces, classified as artificial nanostructured compounds, can exhibit unconventional responses to light in contrast with natural materials, such as high efficiency [1, 2], high bandwidth [3–5], high-quality factor Q [6–8], and perfect absorption [9–11]. Integration of phase change materials (PCMs) with typical optical metasurfaces [12–14] can achieve the real-time tuning of optical resonances and offer promising prospects for multifunctional optoelectronic devices [15, 16]. Vanadium dioxide (VO_2) is an excellent thermal-control material attributed to its low phase-change temperature (around 68 °C), low thermal hysteresis, and high performance in switching cycles. Boyce et al. [13] investigated the plasma dynamic tuning of Au/sub-10 nm-thick VO_2 film structure and confirmed the remarkable stability of the spectra at more than 10 temperature cycles. Kepic et al. [17] constructed VO_2 nanoantennas with tunable Mie resonance in the visible range, exhibiting significant scattering and extinction modulation depth. Ke et al. [18] utilized VO_2 nanoparticles to achieve distinct temperature-response switching. However, VO_2 faces several obstacles, such as weak spectral shift under two states, narrow absorption range, low Q-factor, limited solar modulation [19], and unfavorable brown color. It thus hinders its applications in photoelectric detection [20], perfect absorption, and structural color.

Though high-ε materials have been introduced to enhance the absorption [5], yet studies on the absorption features' tunability still lack. The transition metal dichalcogenides (TMDs) provide one promising solution because of their excitonic absorption, high photoresponsivity, and robust optical coupling [21–25]. It exhibits potential for optical absorption [26], photoluminescence [27, 28], and

***Corresponding authors: Linhua Liu and Jia-Yue Yang**, Optics & Thermal Radiation Research Center, Institute of Frontier and Interdisciplinary Science, Shandong University, Qingdao, 266237, P.R. China; and School of Energy and Power Engineering, Shandong University, Jinan, 250061, P.R. China, E-mail: liulinhua@sdu.edu.cn (L. Liu), jy_yang@sdu.edu.cn (J. Y. Yang). https://orcid.org/0000-0002-3678-827X (J. Y. Yang)
Tao Cheng, Optics & Thermal Radiation Research Center, Institute of Frontier and Interdisciplinary Science, Shandong University, Qingdao, 266237, P.R. China
Yukuan Ma, College of Electronic Information, Sichuan University, Chengdu, 610000, P.R. China
Huanhuan Zhao and Tianhao Fei, School of Energy and Power Engineering, Shandong University, Jinan, 250061, P.R. China

Open Access. © 2023 the author(s), published by De Gruyter. This work is licensed under the Creative Commons Attribution 4.0 International License.

detectors [29]. Previous works [20, 30, 31] have successfully achieved resonant optical absorption by coupling TMDs with VO_2 multilayer metamaterials. Yan et al. [20] achieved active tuning of the collective Mie resonances from silicon nanoparticle clusters by constructing a new platform of VO_2 thin film with a tungsten disulfide (WS_2) sheet. Hou et al. [30] combined molybdenum disulfide (MoS_2) with VO_2 to modulate its photoluminescence. Chen et al. [31] developed a novel model of tunable broadband near-infrared absorber with the help of MoS_2 coupled with VO_2. Most studies have focused on the performance changes by additionally adding TMDs to the VO_2 composite structure. However, the specific ability of TMDs to improve the spectral absorption of VO_2 and the underlying physical mechanisms have been rarely reported, which underestimates the development potential of TMDs–VO_2 composite devices. Furthermore, improving the spectral tunability of the VO_2 composite structure in the visible range can enhance the dynamic control of the structural color [32, 33]. The structural color originates from the interaction between light and complex micro- and nanostructures, involving fundamental optical processes such as diffraction, interference, and scattering [34], and has excellent color and gloss stability and good thermal and chemical resistance. Zhao et al. [32] improved the dynamic tuning of the structural color of VO_2 by varying parameters such as the layer thickness of metal and VO_2. Kim et al. [33] improved the reflected color purity of VO_2 tuning by constructing nanoparticle absorbers. Yet, specific studies of TMDs to modulate VO_2 composite structures' color remain untapped.

Herein, we have investigated the spectral tuning possibility and physical mechanisms of MoS_2/VO_2/Au/Si metasurface in the visible range with the help of spectroscopic ellipsometry (SE) experiments, density functional theory (DFT), and finite-element method (FEM) simulations. First, a multilayer VO_2/Si/Au structure is fabricated, and the spectral properties are obtained with SE. Then the contribution of O-2p electrons in VO_2 to dielectric function at different phases is shown using DFT. The dependence of absorption on temperature and VO_2 thickness is investigated with FEM, obtaining the excitation conditions of Fabry–Perot (F–P) resonance. Furthermore, the MoS_2/VO_2/Si/Au metasurface is designed and found to have a broader range of solid absorption and richer spectral features with modulating incident angle and MoS_2 morphology than the multilayer structure. The electromagnetic field results reveal that the F–P resonances in the VO_2 and MoS_2 layers play a critical role in spectral regulation. Finally, the structural color is studied as an extended application based on spectral modulation and exhibits different sensitivity to temperature, oblique incidence angles, and heights of MoS_2. This work aims to facilitate tuning the VO_2 metamaterial active coupling light and dynamic structural color.

2 Experimental & computational methodology

2.1 Structural design

The VO_2/Au/Si hierarchical structure was fabricated by the magnetron sputtering method as shown in Figure 1a. Real photographic images of the hierarchical structure before and after the phase transition are presented. The structure appears lime green at room temperature and yellowish brown after the phase transition. The sample was characterized by XRD (Rigaku SmartLab 3 kW) with Cu K1 irradiation at a scanning rate of 3°/min with 2θ ranging from 25° to 70°. In the test, the grazing incidence was chosen at an incidence angle of 0.5° because that the high energy of normal incident light easily penetrates the film and reaches the substrate, thus causing a large disturbance to the final result. The peaks at 28.03°, 44.5°, 55.5°, and 64.8° in Figure 1b correspond to the (011) [35], (012) [36], (211) [37], and (013) [36] planes of VO_2, respectively, confirming the existence of monoclinic (M_1) phase transition of VO_2. It is worth noting that there is a 38.5° peak, which is not strictly an Au diffraction peak ((111), 37.9° [35]) nor a VO_2 diffraction peak ((020), 39.9° [37]). This is a mixed peak of the two elements caused by the energy breakdown through the VO_2 film to the Au surface due to the excessive intensity of the light source and the thin thickness of the VO_2 film. The diffraction peaks of other impurities or phases were not detected except for the diffraction peaks of M_1-VO_2 films. The surface morphology (Figure S1) and energy dispersion (Figure 1c) of the samples were also investigated by scanning electron microscope (SEM) – energy dispersive spectroscopy (EDS) model SU8220. The results confirm the presence of V and O elements in the sample. Figure 1c also shows the Au peak caused by the energy breakdown through the VO_2 film.

Figure 1d depicts the experimentally prepared schematic diagram of multilayer VO_2/Au/Si. The total thickness is 1 mm, and the thickness of Au and VO_2 is 150 nm and 123 nm, respectively. In the FEM simulation, the periodic tetragonal structure with a period P of 250 nm × 250 nm is used. The total thickness is set to 700 nm, ensuring that the electromagnetic waves do not penetrate the structure, so the absorption is $A = 1-R$. Figure 1e and f shows the MoS_2/VO_2/Au/Si metasurface, where the MoS_2

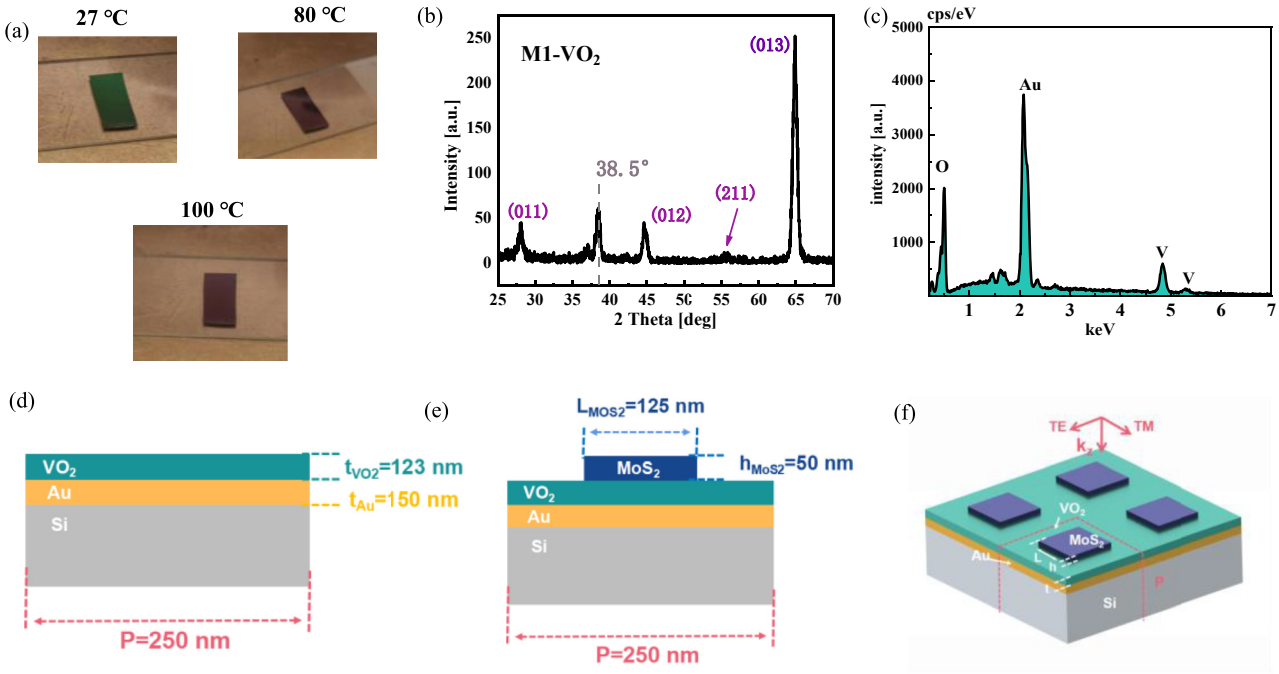

Figure 1: Characterization of the prepared samples and model parameters for calculation. (a) The real optical photograph images of the fabricated VO_2/Au/Si multilayer structure at 27 °C, 80 °C, and 100 °C, respectively. (b) XRD results of VO_2/Au/Si multilayer structure at grazing incidence. (c) EDS spectrum of VO_2/Au/Si multilayer structure. (d) Optical schematic of the hierarchical structure. (e) Parametric diagram and (f) global schematic diagram of MoS_2/VO_2/Au/Si metasurface.

shape is square with default side length and height of $L = 125$ nm and $h = 50$ nm, respectively. The main polarization directions of the light source are transverse electric (TE) and transverse magnetic (TM) directions.

2.2 Experiments and simulations

The reflectivity and temperature-dependent dielectric function of the VO_2/Au/Si hierarchical structure was measured with the RC2 ellipsometer purchased from J.A. Woollam Company. In the high-temperature test, the Linkam heat cell heated the system. The measured angle of incidence was set to 70°. Nitrogen gas was continuously introduced during heating to remove oxygen from the heating chamber to prevent oxidation. The ellipsometric parameters of ψ and Δ were first obtained by RC2 ellipsometer. Each layer was modeled separately for the hierarchical structure to extract its dielectric function and thickness. The silicon substrate layer was modeled first, followed by an intermediate layer of thin-film gold with a thickness of 150 nm. Finally, the VO_2 layer was modeled with the optical model B-spline [38] to improve the fitting accuracy of this layer, and the thickness fitting option was turned on. The dielectric functions of Si, Au, and VO_2 at temperatures ranging from 30 °C to 300 °C in the spectral range of 300 nm–1600 nm were obtained and the thickness of VO_2 obtained by fitting was 123 nm. A more detailed ellipsometric working principle can be found in our previous study [39].

With the SE-measured dielectric function as input, FEM simulations on radiative properties of multilayer structures were performed. Floquet periodic boundary conditions were used in the X and Y directions to mimic the composite structures, and perfect matching layers (PML) boundary conditions were used in the Z direction to truncate the simulation volume. The thickness of PML was set to 1/4 wavelength and the convergence mesh to 1/5 wavelength, respectively.

The impedance transformation method can be applied to analyze the absorption properties of the structure, and the impedance Z of the absorber and impedance Z_0 of free space are calculated following [40, 41]

$$Z = \pm\sqrt{\frac{(1+S_{11})^2 - S_{21}^2}{(1-S_{11})^2 - S_{21}^2}} \tag{1}$$

$$Z_0(\lambda) = \sqrt{\frac{\mu(\lambda)}{\varepsilon(\lambda)}} \tag{2}$$

where S_{11} and S_{21} are the reflection and transmission coefficients, $\mu(\lambda)$ and $\varepsilon(\lambda)$ are the magnetic permeability and dielectric function of the structure at the wavelength, respectively. The closer the impedance of the absorber is to $Z_0 = 1$, the stronger its absorption capacity.

3 Results and discussions

3.1 VO_2/Au/Si hierarchical structure

We first investigate the dielectric function of VO_2 films in the VO_2/Au/Si hierarchical structure. According to previous studies [42, 43], VO_2 undergoes tetragonal rutile (R) phase to M_1 phase transition as the undimerized vanadium atoms undergo classical Mott transition, and the crystal symmetry is broken (Figure S2). This process inherently changes the dielectric function of VO_2, which is closely related to the atomistic and electronic structure, and Figure 2a and Figure S3 illustrate the differences. The onset of the absorption peaks of the absorption coefficient spectrum (α) reflects the optical band gap and can be obtained from the intersection of the tangent line of the absorption edge of the spectral absorption peak with the energy axis (x-axis) [44], as shown in Figure 2b. In VO_2, the absorption onset O of main peak K_1 (Figure 2b) is related to the indirect transition process involving O-2p and V-3d states near the Fermi energy level. And the onset O′ of peak K_2 is contributed by the transition process of O-2p states to higher energy levels (see S4 for more details in Supplementary Information). The temperature dependence of onsets for different absorption peaks is thoroughly investigated. As seen in the inset of Figure 2c, high temperature induces a red-shift of the onset O due to Mott physics [42], i.e., the band gap energy decreases with increasing temperature. In the R phase, the onset O disappears due to the vanishing of the interband transitions between V-3d and O-2p states. On the other hand, the onset O′ of peak K_2 blueshifts with increasing temperature in the M_1 phase indicates an increase in the transition energy of O-2p states. However, after the phase transition occurs, there is a significant red-shift in the absorption onset O′ due to the reduced band gap and lower transition energy of O-2p states to higher energy states (Figure S4a–b). Also, there is an overall decreasing pattern of onset O′ with increasing temperature, which indicates that high temperature causes a decrease in the O-2p states transition energy in the R phase. More relevant details of DFT calculations and discussions are given in Supplementary Information S4.

Next, the radiation characteristics of the multilayer structure are studied using FEM simulations. Since fewer metallic features are involved [45], we call the dielectric states before and after the phase transition high-ϵ and low-ϵ, respectively. Figure 2d shows a considerable polarization sensitivity in the absorption of the hierarchical structure at oblique incidence, so all the absorption mentioned in this paper is total $A_{\text{total}} = (A_{\text{TE}} + A_{\text{TM}})/2$. As seen in Figure 2e, the FEM simulation results agree well with experimental results regarding absorption peak positions, which provides

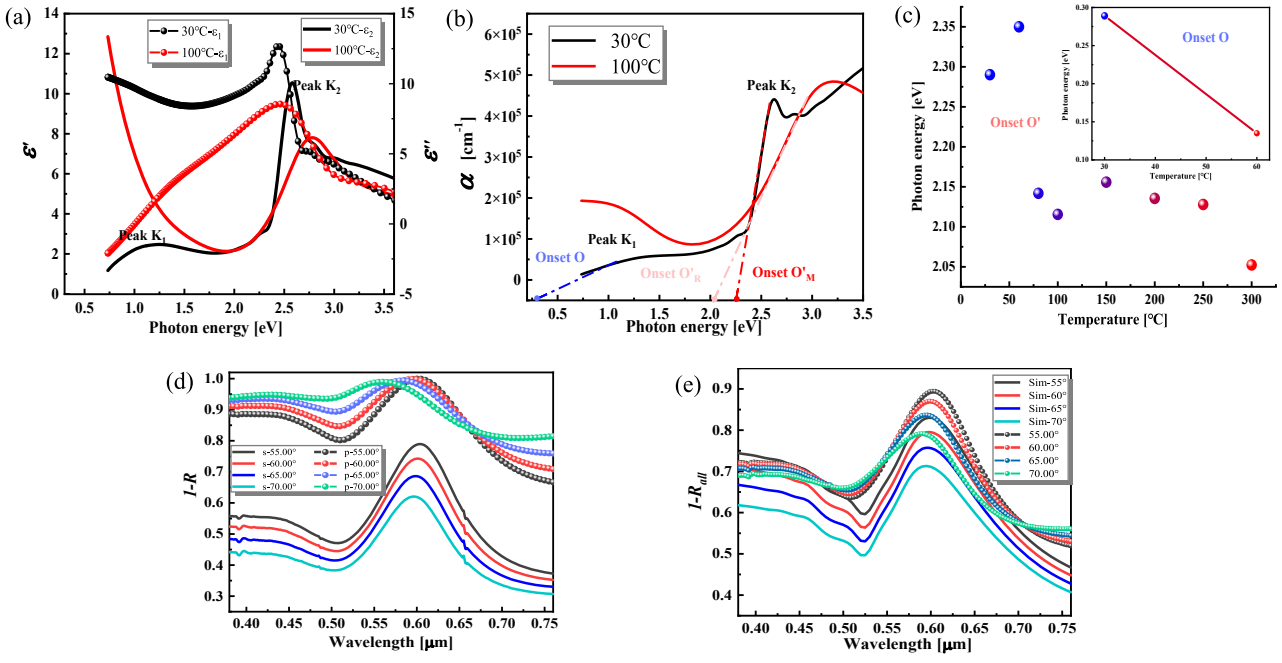

Figure 2: Ellipsometric measurements: (a) VO_2 dielectric function under two phases, (b) VO_2 absorption coefficients under two phases and the location of the marked of absorption onset, (c) absorption onset at different temperatures, (d) absorptance under s (TE) and p (TM) polarization, and (e) the comparison between experimental measurements and FEM calculations.

favorable conditions for the peak coupling study below. However, the absolute value of the simulated absorption is lower than that of the experimental results, possibly due to the deviation of the VO_2 thickness (confirmed by Figure 3b) chosen in the simulation from the actual experiment and errors from the material parameters.

Then, the absorption contribution of each layer in the hierarchical structure is investigated. Figure 3a shows that the VO_2/Au/Si structure has three absorption peaks in the visible range, and they are all contributed by the VO_2 layer, which can be confirmed by comparing the absorption of the VO_2/Si bilayer structure. The Au layer

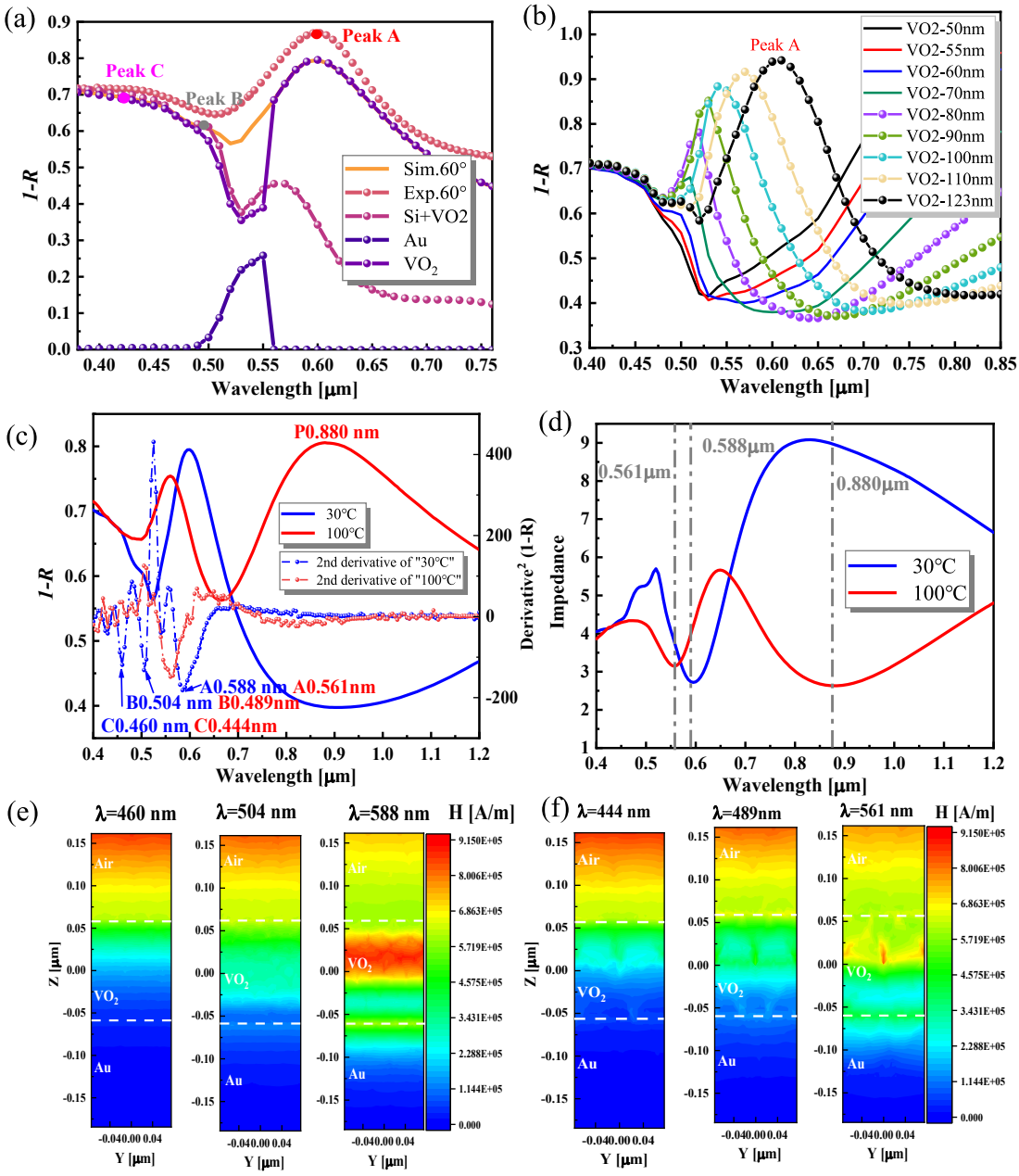

Figure 3: Absorption characteristics of VO_2/Au/Si hierarchical structure. (a) The absorption at 60° incidence, including the VO_2/Au/Si hierarchy (including simulation and experiment), the individual contribution from its components (including Au layer and VO_2 layer), and VO_2/Si bilayer reference structure. (b) Calculation of the thickness dependence of VO_2 at vertical incidence. (c) Absorption of the hierarchy structure at 30 °C and 100 °C at 60° incidence. The positions of absorption peaks A, B, and C at 30 °C and 100 °C are 0.588 nm, 0.504 nm, 0.460 nm and 0.561 nm, 0.489 nm, 0.444 nm, respectively. Dotted lines plots indicate $\frac{\partial^2 A}{\partial \lambda^2}$ at the corresponding temperatures. (d) Impedance ($(Z_{TE} + Z_{TM})/2$) of the hierarchy structure at 30 °C and 100 °C at 60° incidence. Magnetic fields of absorption peaks A, B, and C at (e) 30 °C and (f) 100 °C.

mainly contributes to the 0.46–0.56 μm range absorption. To better distinguish the absorption features, we fit the second derivative of the absorption spectra concerning wavelength $\left(\frac{\partial^2 A}{\partial \lambda^2}\right)$ referring to the previous treatment of enhanced dielectric function spectral line shapes [46, 47] (see S5 for more details in Supplementary Information). Then, the formation conditions of the F–P resonance [20] in VO_2 and its contribution to peak A are studied. The magnetic field (Figure S6) at peak A is localized inside the VO_2, confirming the formation of F–P resonance. Figure 3b shows that as the thickness of VO_2 decreases, the absorption peak A blueshifts and weakens until peak A disappears at the height $h \approx 50$ nm. It is due to the reduction of the effective cavity length and the gradual disappearance of the F–P resonance. The low thickness exhibits a narrower bandwidth, which has lower energy dissipation, as evidenced by the more muscular magnetic field strength (Figure S6).

When VO_2 shifts from high-ε state to low-ε state, peak A blueshifts and decreases in value (Figure 3c). It is due to the weakened F–P resonance, and the magnetic field exhibits a weaker and nonuniform character, as shown in Figure 3e and f. Since A_{TE} is similar to A_{total}, this paper's magnetic and electric fields are considered under the TE wave. In the near-infrared (NIR) range, a plasmonic resonance (peak P) appears attributed to the more active surface electrons in metallic VO_2 [31]. The solid optical interference [30] enhances the total absorption within the spectrum (Vis-NIR region), as shown in Table S1. The impedance transformation method can also be used to analyze the absorption changes of the hierarchical structure caused by the phase transition of VO_2 [48]. As shown in Figure 3d, the low-ε state makes the impedance lower and closer to 1, thus increasing the absorption of the structure. The peak A related to F–P resonance of the low-ε state is blue-shifted concerning the high-ε state, while the impedance value of the low-ε at the dip is higher than that of the high-ε state, indicating a lower absorption capacity. The impedance curve is smoother in the range below 561 nm, which is shown in the absorption curve as the disappearance of the remaining peaks except peak A (Figure 3c). In addition, an impedance dip at the wavelength of 880 nm indicates the appearance of a new absorption.

3.2 MoS_2/VO_2/Au/Si metasurface

The bulk MoS_2 has excellent excitonic polarization that can realize light–matter solid interactions [49], which helps improve the spectral tuning of the VO_2 system. A MoS_2/VO_2/Au/Si simulation model is developed using the default parameter values in Figure 1c and d and studied for the radiation performance. The dielectric function of bulk MoS_2 is available in the literature [27]. Figure 4a shows that the introduction of the bulk MoS_2 broadens the strong absorption range and increases the absorption features, which is attributed to the high-ε property (see Equation (S2) in Supplementary Information) and abundant exciton absorption of MoS_2 (Figure S3e). Peak A red-shifts, and peaks B, C, and E related to MoS_2 excitons emerge, suggesting the enhanced average optical absorption (from 0.54 up to 0.65 in the 400 nm–1000 nm range). Peak D contributed by MoS_2 blueshifts slightly and increases in amplitude. Figure 4b–d demonstrates the specific physical mechanism. The magnetic fields at peaks A, B, and C show a longer optical path and are located in the middle region between the lower MoS_2 layer and the upper VO_2 layer, demonstrating that a new F–P resonance is generated in MoS_2 [20], where the Au layer and the top MoS_2 act as two reflectors. The optical field at peak D is strongly localized at the MoS_2 surface edge, and the internal field strength is also more extensive than that of the pure VO_2 structure (Figure 4c and d), explaining the high value (see Equation (S2) in Supplementary Information) and the narrow bandwidth of peak D.

Furthermore, the effect of the polarization and incidence angles on the MoS_2 metasurface is investigated. The sensitivity of the metasurface to the polarization angle is first studied, as shown in Figure S7a–d. When averaging the absorption of the TE and TM directions at an oblique incidence angle of 60°, it is found that in the 0°–80° polarization range, the absorption shows a symmetric distribution with the polarization angle of 40° as the dividing line, i.e., the closer to 40° polarization angle, the larger the absorption of the metasurface. Then, the sensitivity of the metasurface to the incidence angle is investigated. As shown in Figure 5a and e, peak A decreases with increasing angle, while the absorption in the range from peak E to peak B position shows the first increase and then decreases with increasing angle, and the turning point of the change is near 30°. It is evidenced by the weaker optical field of peak B at a larger angle (>30°), as shown in Figure S7e. The contour plot of total absorption (contour plots of absorption in the TE and TM directions are shown in Figure S8a and S8b in Supplementary Information) shows that the dip X becomes apparent around 35°, which derives from the blueshift and decreases in the bandwidth of peaks E and D with increasing angle. The peak X (at $\lambda = 544$ nm) is smoothed to annihilation at an increasing angle of 50°, which the more divergent magnetic field can explain at a higher angle (Figure S7f). In a word, the incidence angles can improve the spectral modulation performance of the

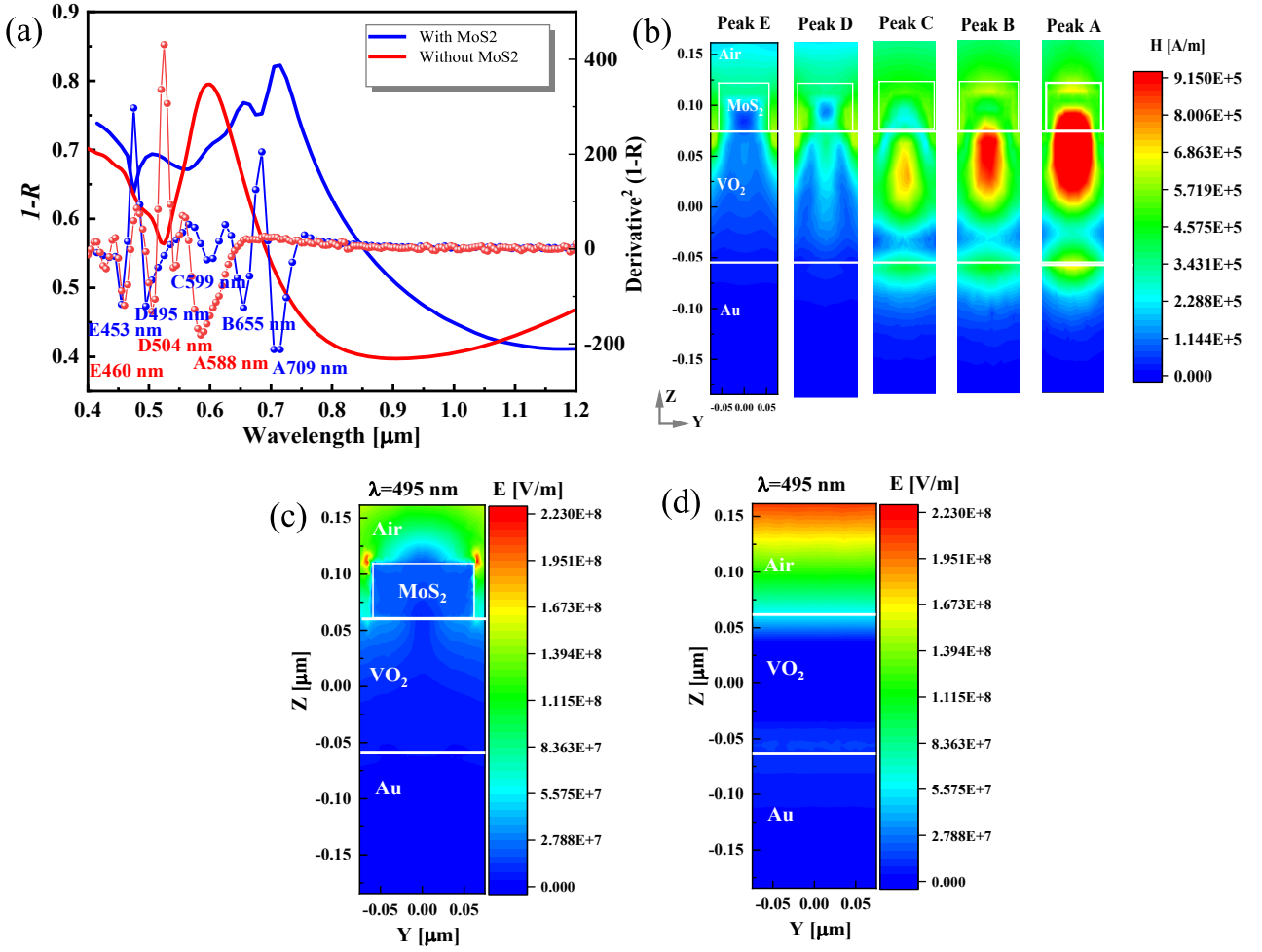

Figure 4: Absorption characteristics of $MoS_2/VO_2/Au/Si$ metasurface. (a) Comparison of absorption of structures with and without MoS_2 at an oblique incidence angle of 60°. The size of MoS_2 is the default structural parameter. Dotted lines plots indicate $\frac{\partial^2 A}{\partial \lambda^2}$ at the corresponding structure. (b) The magnetic fields at different peaks of the structure with MoS_2. (c) Optical field of peak D ($\lambda = 495$ nm) under MoS_2 nanostructure. (d) Optical field of D under VO_2/Au/Si structure.

metasurface and realize the free transition between multiple peaks and dips.

The excitonic features of MoS_2 determine the absorption of the metasurface, and the height affects the performance of the excitonic mode, so the optical absorption related to the height of MoS_2 is further investigated. The finite-thickness MoS_2 weakly increases the absorption and optical fields of the structure (Figure S9a–b). However, as the bulk MoS_2 thickness increases to about 35 nm, peak A keeps red shifting and splitting, and its slight dip feature at $\lambda = 660$ nm turns into a peak (B) feature (Figure 5b and f). This is due to increased excitonic mode coupling specific gravity [50], which induces the Fano resonance. In this process, the quality of peak C ($\lambda = 612$ nm) also becomes apparent and no longer varies with height. The $\left(\frac{\partial^2 A}{\partial \lambda^2}\right)$ shows more information on the displacement of the absorption peaks with height (Figure S9c). In addition, the absorption increases with height, and the average absorption in the visible region (380–760 nm) reaches 0.9 when $h = 70$ nm (angle = 0°). A nearly perfect absorption of 0.9992 can be achieved at $\lambda = 735$ nm. This is due to the increased effective cavity length and the enhancement of the optical interference [30]. The magnetic fields are more localized at the higher height in the MoS_2 nanostructure (Figure S10), where the excitons coupling is enhanced. It proves that the F–P resonance is also generated in MoS_2 at long wavelengths at a certain height.

The length of MoS_2 (L) determines the responsiveness of the nanostructure to light. Therefore, maintaining the period $P = 250$ nm unchanged, the effect of MoS_2 size on the metasurface's optical absorption is investigated. Figure 5c–g show that the dominant peak A exhibits a significant red-shift and decreases in amplitude as L increases. When L increases to 140 nm, a new absorption peak N

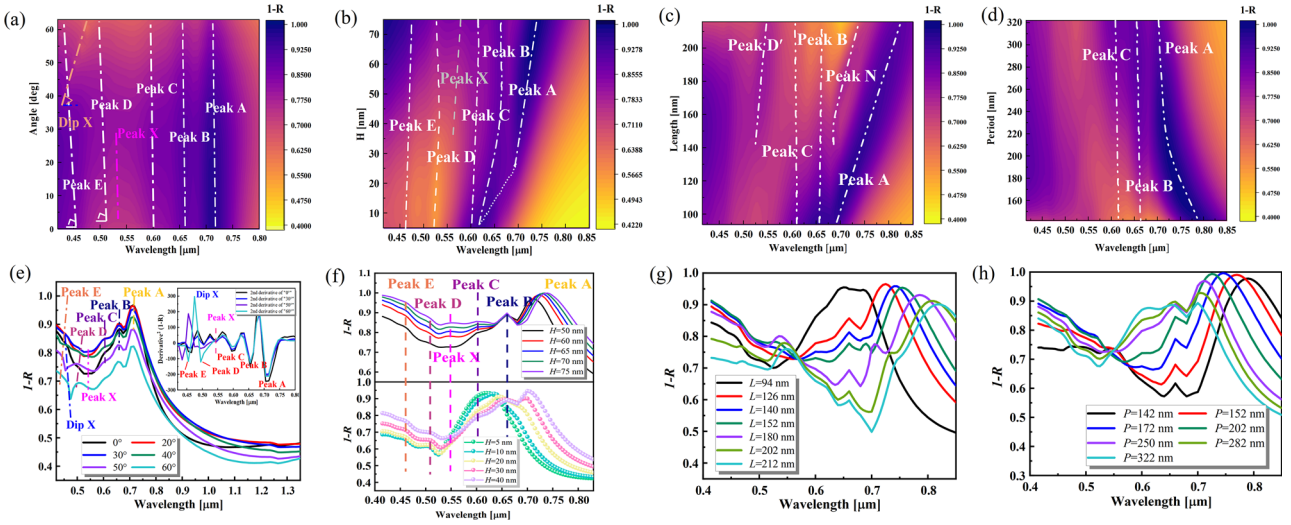

Figure 5: Contour map of absorption A_{total} dependent on structural morphology. (a) Calculated A_{total} contour map at different angles. (b) Calculated height-dependent absorption A_{total} contour map of MoS_2 at vertical incidence. (c) Calculated length-dependent absorption A_{total} contour map of MoS_2 at vertical incidence, $P = 250$ nm. (d) Calculated period-dependent absorption A_{total} contour map of metasurface at vertical incidence, $L = 125$ nm. (e) A_{total} of metasurfaces at different angles. The inset shows the $\frac{\partial^2 A}{\partial \lambda^2}$ at the corresponding angles. (f) Calculated absorption at different MoS_2 heights at vertical incidence. (g) Calculated absorption at different MoS_2 lengths at vertical incidence, $P = 250$ nm. (h) Calculated absorption at different metasurface periods at vertical incidence, $L = 125$ nm.

appears near $\lambda = 680$ nm and shows a trend of feature enhancement followed by weakening as L increases. This feature can be interpreted with the help of the optical field, as shown in Figure S11. At this time, the strong magnetic field is contributed by the upper surface and lower surface (MoS_2/VO_2 intersection) of MoS_2. The optical field is mainly localized around the MoS_2 bottom corner between adjacent cells, and the MoS_2 interior also contributes a part of the field strength. In addition, when L increases to 142 nm, the absorption peak D′ at $\lambda = 520$ nm becomes gradually apparent. By observing its optical and magnetic field distribution, one can find that the peak D′ is very similar to D contributed by MoS_2 mentioned above (see S13 for more details in Supplementary Information). Then, keeping the MoS_2 size $L = 125$ nm unchanged, the period (P) variation on the metasurface absorption properties is investigated. First, the changes in the period do not produce new absorption features (peaks or dips). As the period increases, the prominent peak A blue shifts, and its broadening decreases. The peaks of exciton peaks B and C increase, and their broadening increases. By defining the filling factor $FF = (L/P)^2$ [51] for the metasurface, it is observed that the absorption peak A red-shifts markedly and the exciton peaks B and C decrease with increasing filling factor.

The effect of VO_2 phase transition on absorption is further investigated, as shown in Figure 6a. When VO_2 changes from high-ε state to low-ε state, the absorption peaks blueshift, and peak A couples with peak B to produce a blue-shifted peak B′ with a higher value. The quality factors Q (see Equation (S3) in Supplementary Information) [50] before and after coupling are 9.39 and 52.57, respectively, with a ratio of 5.60. It proves the occurrence of stronger coupling (see S14 for more details in Supplementary Information). The F–P resonances in peaks A, B, and C move from the VO_2 layer to the MoS_2 layer, where the VO_2 layer mainly acts as a reflector (Figure S14a). Also, the mean value of the metasurface's absorption in the visible range decreases from 0.75 to 0.74, opposite to the temperature dependence of the VO_2/Au/Si structure's absorption. The impedance analysis shows that the Z of low-ε state increases in the wavelength range of 646–756 nm and further away from 1, which is the main reason for the lower average absorption in the visible range (Figure 6b). In the low-ε state, a plasmon resonance peak P is formed in the NIR region, and the relationship between the plasmon resonance and the bulk MoS_2 side length L is investigated, as shown in Figure 6c. The peak P red-shifts and increases bandwidth with increasing L of MoS_2. It can be explained by the expansion of the magnetic field from the MoS_2 layer to the VO_2 layer (raised optical path) and by the diverging magnetic field (Figure S14b). As L increases, the peak P value increases and then decreases, reaching a maximum at $L = 140$ nm, which can be verified by the average optical field value trend (Figure S14c).

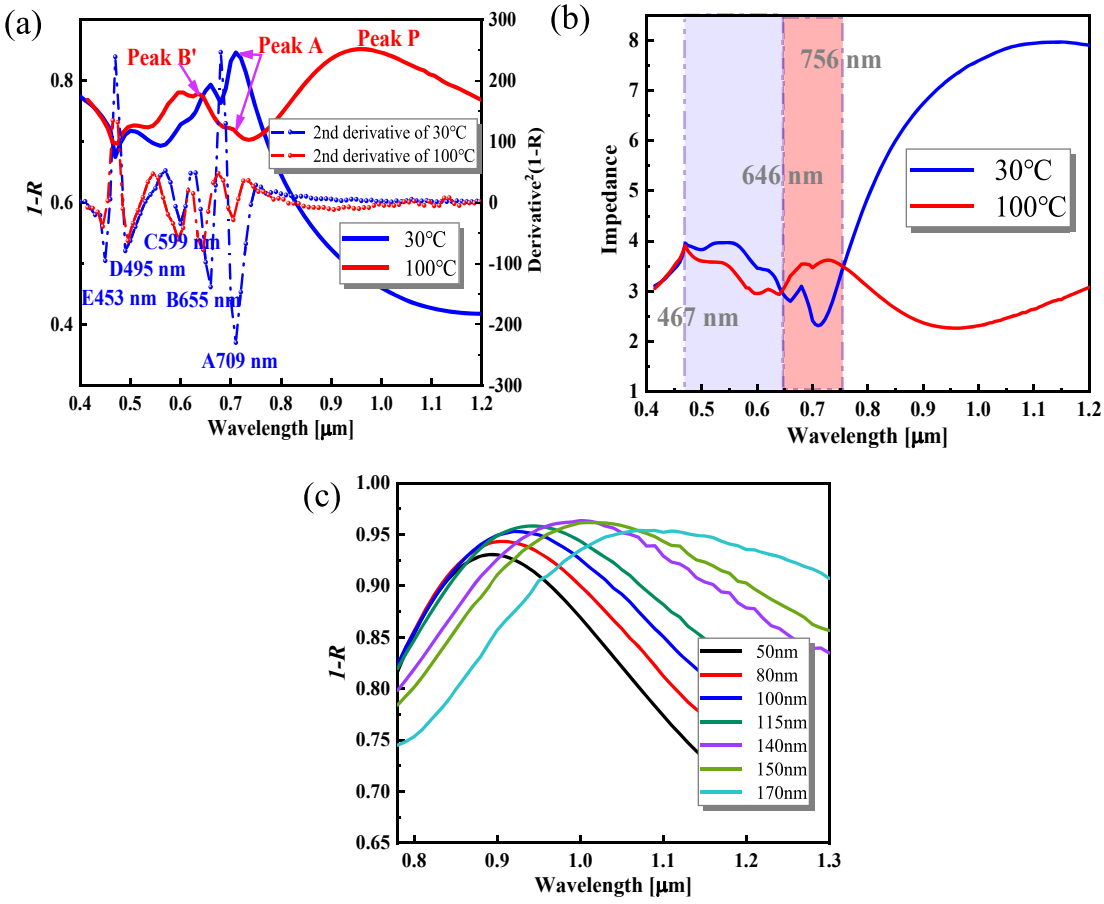

Figure 6: Absorption of $MoS_2/VO_2/Au/Si$ metasurface effected by VO_2 phases transition. (a) Comparison of calculated absorption in the high-ε state and the low-ε state at an oblique incidence angle of 60°. Dotted lines plots indicate $\frac{\partial^2 A}{\partial \lambda^2}$ at the corresponding structure. (b) Impedance $((Z_{TE} + Z_{TM})/2)$ of the MoS_2 metasurface at 30 °C and 100 °C at 60° incidence. (c) Variation of plasmonic resonance peaks with MoS_2 side length L.

3.3 Modulation of structural color

The above results suggest that the temperature, oblique incidence angle, and morphology improve the metasurface system's light–matter interactions and that structural color's dynamic regulation potential is accordingly stimulated [34]. First, the effects of temperature and VO_2 thickness on the structural color are investigated. Based on the temperature-dependent dielectric function, the reflectance spectra of the $VO_2/Au/Si$ structure in the visible range at different temperatures are obtained by dispersion relations [52]. The phase transition caused a blue shift in the spectrum with decreased absorption amplitude (Figure S15a). The data in the CIE chromaticity diagram intuitively represent the variations of color coordinates from (0.2281, 0.2128) to (0.3199, 0.2710) with increasing temperature from 30 °C to 100 °C (Figure 7a). Then, the color coordinates do not change with temperature. During this process, the brightness decreases from 0.9078 to 0.8784, with a change of 0.0294. The saturation decreases from 0.8724 to 0.3459, with a change of 0.5175. The color changes from aquamarine (Hue:8.7804°) to pink (Hue:128.185°). Figure 7b shows the color comparison between the FEM calculation and experiment, with an average error of 0.02415 in the coordinate positions, which is suitable for subsequent variable analyses. Next, we compared the difference in the effect of structural color on VO_2 thickness due to phase transition by numerical calculation. More details of the calculations and analysis are shown in Supplementary Information S16. The results indicate that with increasing VO_2 thickness at the normal incidence, the maximum variations of brightness and hue in the high-ε state are more prominent than that in the low-ε state, while the maximum variation of saturation is the opposite.

The sensitivities of the structural color of $MoS_2/VO_2/Au/Si$ metasurfaces to the oblique incidence angles and heights of the MoS_2 are investigated. Figure 7c shows that as the MoS_2 height increases from $h = 0$ nm to

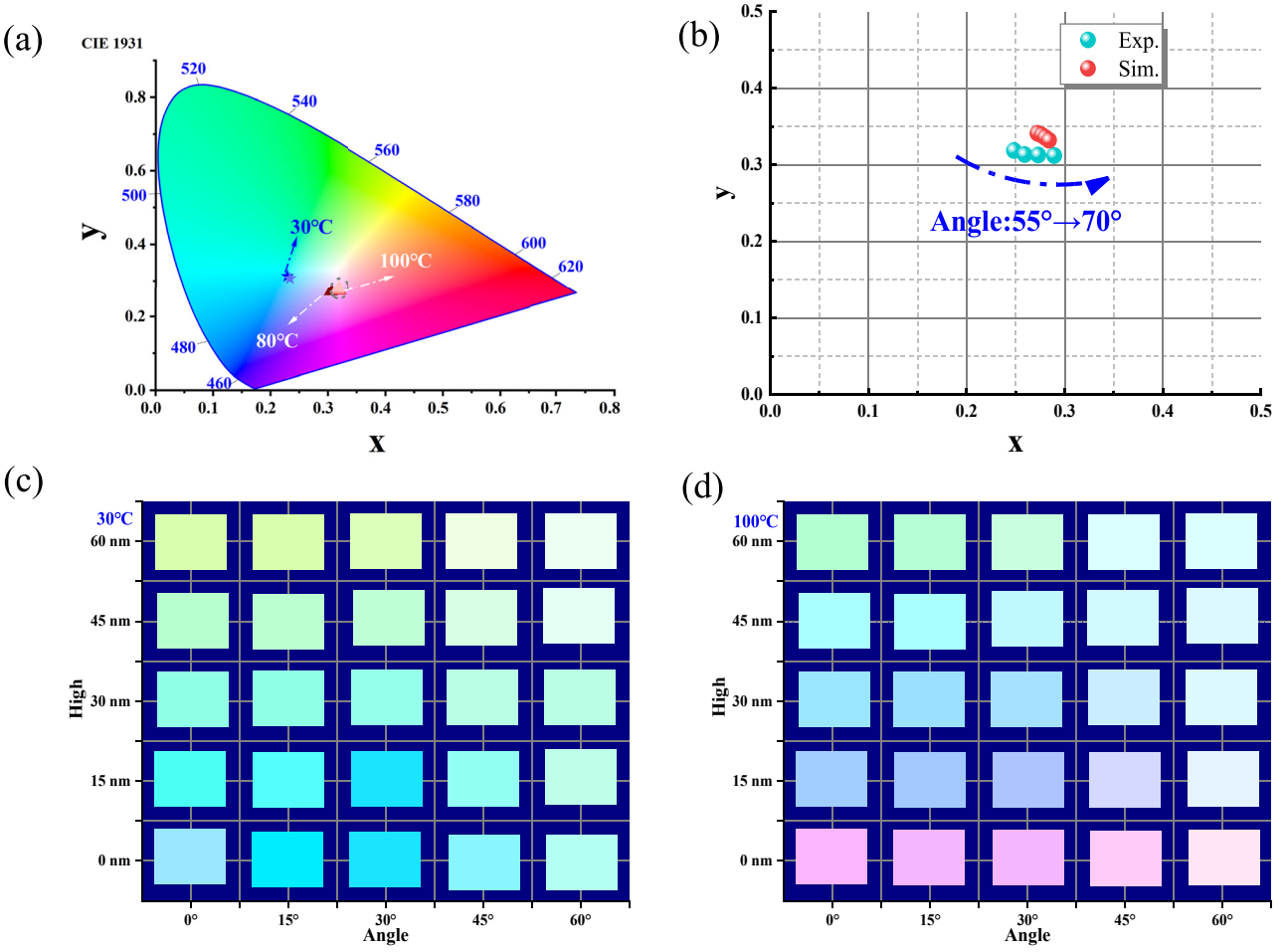

Figure 7: Structural color characteristics of the MoS_2/VO_2/Au/Si metasurface. (a) Data points in the CIE chromaticity diagram at different temperatures. The data in Figure S12a provide the raw spectral information. (b) Comparison of experimental data with FEM simulation data in x–y coordinates. The color palette of the reflective colors as a function of the thicknesses of MoS_2 layers and oblique incidence angles at (c) 30 °C and (d) 100 °C.

$h = 60$ nm at an oblique incidence angle of 15°, the brightness increases from 0.32 to 0.4863 ($h = 45$ nm) and then decreases to 0.409 ($h = 60$ nm), with a maximum variation of 0.164. The hue falls from 183.5955° to 87.6893°, with a maximum variation of 96.206°. The saturation decreases from 1 to 0.1866, with a maximum variation of 0.8134. When the oblique incidence angle is 60°, the maximum variation values of brightness, hue, and saturation are 0.045, 49.5°, and 0.155, respectively. It indicates that the three attributes of color are all more sensitive to heights at low incidence angles. Fixed the height $h = 15$ nm, as the oblique incidence angle increases from 0° to 60°, the brightness first decreases from 0.4412 to 0.3863 (Angle = 30°) and then increases to 0.5686 (Angle = 60°), with a maximum variation of 0.1823. The hue increases from 176.5048° to 180° (Angle = 30°) and then decreases to 160.5°, with a maximum variation of 19.5°, corresponding to the turning trend of the variable angle spectra (Figure 5a–e). The saturation increases from 0.4578 to 0.4882 (Angle = 15°) and then decreases to 0.1818 with a maximum variation of 0.3064. When the height $h = 60$ nm, the maximum variation of brightness, hue, and saturation are 0.1647, 34.29°, and 0.1648, respectively. It indicates that the angular sensitivities of brightness and saturation are more significant at low heights, while the hue is the opposite. On the other hand, Figure 7 shows that the sensitivities of brightness and hue to height are more significant at low incidence angles in the low-ε state, while the trend for saturation is reversed. In addition, brightness and saturation are more sensitive to angle at low heights, while hue has the opposite direction. Furthermore, the sensitivities of structural color' attributes to the temperature are consistent with the above findings (see S16 for more details in Supplementary Information). For example, the hue caused by the height of MoS_2 in the low-ε

state has a more pronounced change than the high-ϵ state, which can be visualized by comparing the color changes in the bottom two rows of Figure 7c and d, respectively. Table S2 in the Supplementary Information gives the RGB values under each structure with the corresponding detailed brightness, hue, and saturation values for the reader's reference.

4 Conclusions

In summary, we present a MoS_2/VO_2/Au/Si metasurface with dynamic spectral tuning and reveal the modulation mechanism employing optical, magnetic field analysis, and impedance matching theory. The spectra of multilayer structures are first obtained by SE experiment. DFT results show that the onset of dielectric absorption peak K_2 of VO_2 is related to the O-2p state's transition and has opposite responses to temperature in different phases. FEM simulations show that F−P resonance generated in VO_2 and MoS_2 dominates the metasurface's absorption properties and is sensitive to the excitation of high temperature, oblique incidence angle, and morphology. Compared to the VO_2 hierarchical structure, the metasurface can provide more than 2–3 times the absorption features, broaden the range of intense absorption, and increase the spectral absorption due to the high ϵ'' properties and rich exciton features of MoS_2. For example, an average absorption greater than 0.9 and near-perfect absorption of 0.9992 can be achieved in the Vis range. On the other hand, spectral perturbations in the Vis range affect the three attributes of the structural color. Most color performances exhibit higher sensitivity to external excitation in the high-ϵ state, at low oblique incidence angles, and at low heights of MoS_2. Such design can also be applied to studying other TMDs materials coupled to VO_2 or expanded into more complex material systems. This work offers fundamental ideas for enhancing the response to light and dynamic tuning of structural color, which can provide exciting applications for optical switching, tunable light detection, temperature sensing, etc.

Supporting Information

Experimental dielectric functions of VO_2, Au, and Si; details of the density functional theory (DFT) calculations and discussions; second-order derivative spectra of the absorption to wavelength; conditions for the formation of F−P resonance in VO_2 and MoS_2; polarization angles dependence and incidence angles dependence (TM and TE) of absorption; electromagnetic field distribution of metasurface at different oblique incidence angles and heights of MoS_2; coupling of absorption peaks due to VO_2 phase change; experimental spectra and structural colors in low-ϵ state; the RGB values under each structure with the corresponding detailed values of brightness, hue, and saturation.

Author contributions: All authors have accepted responsibility for the entire content of this manuscript and approved its submission

Research funding: The National Natural Science Foundation of China (Grant no. 52076123) and Shandong University Outstanding Scholar (Grant no. 82363194).

Conflict of interest statement: Authors state no conflicts of interest.

Data availability: The datasets generated and/or analyzed during the current study are available from the corresponding author upon reasonable request.

References

[1] G. Zheng, H. Mühlenbernd, M. Kenney, G. Li, T. Zentgraf, and S. Zhang, "Metasurface holograms reaching 80% efficiency," *Nat. Nanotechnol.*, vol. 10, no. 4, pp. 308−312, 2015.

[2] M. Feng, B. Zhang, H. Ling, et al., "Active metal−graphene hybrid terahertz surface plasmon polaritons," *Nanophotonics*, vol. 11, no. 14, pp. 3331−3338, 2022.

[3] L. Lei, S. Li, H. Huang, K. Tao, and P. Xu, "Ultra-broadband absorber from visible to near-infrared using plasmonic metamaterial," *Opt. Express*, vol. 26, no. 5, pp. 5686−5693, 2018.

[4] W. Wang, Y. Qu, K. Du, et al., "Broadband optical absorption based on single-sized metal-dielectric-metal plasmonic nanostructures with high-ε″ metals," *Appl. Phys. Lett.*, vol. 110, no. 10, p. 101101, 2017.

[5] Y. Huang, L. Liu, M. Pu, X. Li, X. Ma, and X. Luo, "A refractory metamaterial absorber for ultra-broadband, omnidirectional and polarization-independent absorption in the UV-NIR spectrum," *Nanoscale*, vol. 10, no. 17, pp. 8298−8303, 2018.

[6] N. Liu, M. Mesch, T. Weiss, M. Hentschel, and H. Giessen, "Infrared perfect absorber and its application as plasmonic sensor," *Nano Lett.*, vol. 10, no. 7, pp. 2342−2348, 2010.

[7] Z. Yong, S. Zhang, C. Gong, and S. He, "Narrow band perfect absorber for maximum localized magnetic and electric field enhancement and sensing applications," *Sci. Rep.*, vol. 6, no. 1, p. 24063, 2016.

[8] A. Tittl, A. Leitis, M. Liu, et al., "Imaging-based molecular barcoding with pixelated dielectric metasurfaces," *Science*, vol. 360, no. 6393, pp. 1105−1109, 2018.

[9] J. Wu, Y. Sun, B. Wu, C. Sun, and X. Wu, "Broadband and wide-angle solar absorber for the visible and near-infrared frequencies," *Sol. Energy*, vol. 238, pp. 78−83, 2022.

[10] Y. Li, J. Lin, H. Guo, W. Sun, S. Xiao, and L. Zhou, "A tunable metasurface with switchable functionalities: from perfect transparency to perfect absorption," *Adv. Opt. Mater.*, vol. 8, no. 6, p. 1901548, 2020.

[11] Z. Liu, G. Duan, H. Duan, and Z. Wang, "Nearly perfect absorption of solar energy by coherent of electric and magnetic polaritons," *Sol. Energy Mater. Sol. Cells*, vol. 240, p. 111688, 2022.
[12] L. Lu, Z. Dong, F. Tijiptoharsono, et al., "Reversible tuning of Mie resonances in the visible spectrum," *ACS Nano*, vol. 15, no. 12, pp. 19722—19732, 2021.
[13] A. M. Boyce, J. W. Stewart, J. Avila, et al., "Actively tunable metasurfaces via plasmonic nanogap cavities with sub-10-nm VO2 films," *Nano Lett.*, vol. 22, no. 9, pp. 3525—3531, 2022.
[14] S. Abdollahramezani, O. Hemmatyar, H. Taghinejad, et al., "Tunable nanophotonics enabled by chalcogenide phase-change materials," *Nanophotonics*, vol. 9, no. 5, pp. 1189—1241, 2020.
[15] E. E. Chain, "Optical properties of vanadium dioxide and vanadium pentoxide thin films," *Appl. Opt.*, vol. 30, no. 19, pp. 2782—2787, 1991.
[16] Z. Yang, C. Ko, and S. Ramanathan, "Oxide electronics utilizing ultrafast metal-insulator transitions," *Annu. Rev. Mater. Sci.*, vol. 41, no. 1, pp. 337—367, 2011.
[17] P. Kepič, F. Ligmajer, M. Hrtoň, et al., "Optically tunable Mie resonance VO2 nanoantennas for metasurfaces in the visible," *ACS Photonics*, vol. 8, no. 4, pp. 1048—1057, 2021.
[18] Y. Ke, X. Wen, D. Zhao, R. Che, Q. Xiong, and Y. Long, "Controllable fabrication of two-dimensional patterned VO(2) nanoparticle, nanodome, and nanonet arrays with tunable temperature-dependent localized surface plasmon resonance," *ACS Nano*, vol. 11, no. 7, pp. 7542—7551, 2017.
[19] Y. Ke, I. Balin, N. Wang, et al., "Two-dimensional SiO2/VO2 photonic crystals with statically visible and dynamically infrared modulated for smart window deployment," *ACS Appl. Mater. Interfaces*, vol. 8, no. 48, pp. 33112—33120, 2016.
[20] J. Yan, Y. Li, Z. Lou, C. Ma, G. Yang, and B. Li, "Active tuning of Mie resonances to realize sensitive photothermal measurement of single nanoparticles," *Mater. Horiz.*, vol. 7, no. 6, pp. 1542—1551, 2020.
[21] S. Manzeli, D. Ovchinnikov, D. Pasquier, O. V. Yazyev, and A. Kis, "2D transition metal dichalcogenides," *Nat. Rev. Mater.*, vol. 2, no. 8, pp. 1—15, 2017.
[22] L.-Y. Xie and J.-M. Zhang, "The structure, electronic, magnetic and optical properties of the Mn doped and Mn-X (X = F, Cl, Br, I and At) co-doped monolayer WS2: a first-principles study," *J. Alloys Compd.*, vol. 702, pp. 138—145, 2017.
[23] H. Luo, B. Wang, E. Wang, et al., "Phase-transition modulated, high-performance dual-mode photodetectors based on WSe2/VO2 heterojunctions," *Appl. Phys. Rev.*, vol. 6, no. 4, p. 041407, 2019.
[24] S. Wang, S. Li, T. Chervy, et al., "Coherent coupling of WS2 monolayers with metallic photonic nanostructures at room temperature," *Nano Lett.*, vol. 16, no. 7, pp. 4368—4374, 2016.
[25] L.-Y. Zhao, H. Wang, T.-Y. Liu, F.-F. Li, Q. Zhou, and H.-Y. Wang, "Tailoring photoluminescence of WS2-microcavity coupling devices in broad visible range," *Nanophotonics*, vol. 12, no. 4, pp. 753—760, 2023.
[26] A. K. M. Newaz, D. Prasai, J. I. Ziegler, et al., "Electrical control of optical properties of monolayer MoS2," *Solid State Commun.*, vol. 155, pp. 49—52, 2013.
[27] G. A. Ermolaev, Y. V. Stebunov, A. A. Vyshnevyy, et al., "Broadband optical properties of monolayer and bulk MoS2," *NPJ 2D Mater. Appl.*, vol. 4, no. 1, pp. 1—6, 2020.
[28] Y. Zhang, T. Oka, R. Suzuki, J. Ye, and Y. Iwasa, "Electrically switchable chiral light-emitting transistor," *Science*, vol. 344, no. 6185, pp. 725—728, 2014.
[29] B. Cho, J. Yoon, S. K. Lim, et al., "Chemical sensing of 2D graphene/MoS2 heterostructure device," *ACS Appl. Mater. Interfaces*, vol. 7, no. 30, pp. 16775—16780, 2015.
[30] J. Hou, X. Wang, D. Fu, et al., "Modulating photoluminescence of monolayer molybdenum disulfide by metal—insulator phase transition in active substrates," *Small*, vol. 12, no. 29, pp. 3976—3984, 2016.
[31] J. Chen, F. Tang, X. Wang, et al., "High efficiency broadband near-infrared absorbers based on tunable SiO2-VO2-MoS2 multilayer metamaterials," *Results Phys.*, vol. 26, p. 104404, 2021.
[32] J. Zhao, Y. Zhou, Y. Huo, B. Gao, Y. Ma, and Y. Yu, "Flexible dynamic structural color based on an ultrathin asymmetric Fabry-Perot cavity with phase-change material for temperature perception," *Opt. Express*, vol. 29, no. 15, pp. 23273—23281, 2021.
[33] S. J. Kim, D. Lee, J. Y. Chae, et al, "Reconfigurable, vivid reflective colors based on solution-processed Fabry-Perot absorber using thermochromic vanadium dioxide," *Appl. Surf. Sci.*, vol. 565, p. 150610, 2021.
[34] X. Hou, F. Li, Y. Song, and M. Li, "Recent progress in responsive structural color," *J. Phys. Chem. Lett.*, vol. 13, no. 13, pp. 2885—2900, 2022.
[35] A. L. S. Hassein-Bey, S. Lafane, H. Tahi, et al., "Substrate effect on structural, microstructural and elemental microcomposition of vanadium dioxide thin film," *Marefa Rev.*, vol. 2, pp. 24—28, 2017.
[36] J. Hou, W. Zhongping, D. Zejun, Z. Zhang, and J. Zhang, "Facile synthesize VO 2 (M1) nanorods for a low-cost infrared photodetector application," *Sol. Energy Mater. Sol. Cells*, vol. 176, pp. 142—149, 2018.
[37] C. Wu, Y. Wang, and G. Ma, "Microfabrication of VO2 thin films via a photosensitive sol-gel method," *Coatings*, vol. 11, p. 1264, 2021.
[38] J. W. Weber, T. A. R. Hansen, M. C. M. van de Sanden, and R. Engeln, "B-spline parametrization of the dielectric function applied to spectroscopic ellipsometry on amorphous carbon," *J. Appl. Phys.*, vol. 106, no. 12, p. 123503, 2009.
[39] T. Cheng, T. Fei, W. Zhang, J.-Y. Yang, and L. Liu, "Ellipsometric and first-principles study on temperature-dependent UV—Vis dielectric functions of GaN," *Appl. Opt.*, vol. 60, no. 23, pp. 6869—6877, 2021.
[40] D. Smith, R. Dalichaouch, N. Kroll, S. Schultz, S. McCall, and P. Platzman, "Photonic band-structure and defects in one and 2 dimensions," *J. Opt. Soc. Am. B*, vol. 10, pp. 314—321, 1993.
[41] D. R. Smith, D. C. Vier, T. Koschny, and C. M. Soukoulis, "Electromagnetic parameter retrieval from inhomogeneous metamaterials," *Phys. Rev. E*, vol. 71, no. 3, p. 036617, 2005.
[42] W. H. Brito, M. C. O. Aguiar, K. Haule, and G. Kotliar, "Metal-Insulator transition in VO_2:A DFT+DMFT perspective," *Phys. Rev. Lett.*, vol. 117, no. 5, p. 056402, 2016.
[43] M. Eaton, A. Catellani, and A. Calzolari, "VO(2) as a natural optical metamaterial," *Opt. Express*, vol. 26, no. 5, pp. 5342—5357, 2018.
[44] G. Mannino, I. Deretzis, E. Smecca, et al., "Temperature-dependent optical band gap in CsPbBr3, MAPbBr3, and FAPbBr3 single crystals," *J. Phys. Chem. Lett.*, vol. 11, no. 7, pp. 2490—2496, 2020.
[45] J. Yan, C. Ma, Y. Huang, and G. Yang, "Dynamic radiative tailoring based on mid-refractive dielectric nanoantennas," *Nanoscale Horiz.*, vol. 4, no. 3, pp. 712—719, 2019.

[46] T. J. Kim, S. Y. Hwang, J. S. Byun, N. S. Barange, H. G. Park, and Y. D. Kim, "Temperature dependent dielectric function and the E0 critical points of hexagonal GaN from 30 to 690 K," *AIP Adv.*, vol. 4, no. 2, p. 027124, 2014.
[47] G. Mannino, I. Deretzis, E. Smecca, et al., "CsPbBr3, MAPbBr3, and FAPbBr3 bromide perovskite single crystals: interband critical points under dry N2 and optical degradation under humid air," *J. Phys. Chem. C*, vol. 125, no. 9, pp. 4938—4945, 2021.
[48] H. Liu, Q. Ai, and M. Xie, "Thermally and electrically tunable narrowband absorber in mid-infrared region," *Int. J. Therm. Sci.*, vol. 171, p. 107225, 2022.
[49] D. T. Vu, N. Matthaiakakis, H. Saito, and T. Sannomiya, "Exciton-dielectric mode coupling in MoS2 nanoflakes visualized by cathodoluminescence," *Nanophotonics*, vol. 11, no. 9, pp. 2129—2137, 2022.
[50] G. Zengin, M. Wersäll, S. Nilsson, T. J. Antosiewicz, M. Käll, and T. Shegai, "Realizing strong light-matter interactions between single-nanoparticle plasmons and molecular excitons at ambient conditions," *Phys. Rev. Lett.*, vol. 114, no. 15, p. 157401, 2015.
[51] Y. Chen, Y. Francescato, J. D. Caldwell, et al., "Spectral tuning of localized surface phonon polariton resonators for low-loss mid-IR applications," *ACS Photonics*, vol. 1, no. 8, pp. 718—724, 2014.
[52] C. F. Bohren and D. R. Huffman, *Absorption and Scattering of Light by Small Particles*, New York, John Wiley & Sons, 2008.

Supplementary Material: This article contains supplementary material (https://doi.org/10.1515/nanoph-2023-0169).